FMCW Inverse Circular Synthetic Aperture Radar Using a Fast Time-Domain Reconstruction

Aditya Varma Muppala, *Graduate Student Member, IEEE*, Jeffrey A. Fessler, *Fellow, IEEE*, and Kamal Sarabandi, *Life Fellow, IEEE*

Abstract—This article proposes a millimeter-wave inverse circular synthetic aperture radar system and a fast time-domain wavefront reconstruction (TDWR) algorithm for near real-time, low-cost imaging of packages and concealed objects. An 80-GHz frequency-modulated continuous-wave (FMCW) radar illuminates targets on a high-speed rotating turntable driven by a precision motor system. Data are collected over a synthetic circular aperture and processed to form high-resolution images of targets. To achieve real-time operation, a fast and accurate time-domain reconstruction and deconvolution imaging algorithm is proposed. The image formation is based on frequency-domain wavefront reconstruction for circular arrays that is adapted to FMCW radars by proposing an analogous time-domain approach. Next, an analytical form for the point spread function (PSF) of circular synthetic aperture radars (CSARs) is derived and used to speed up the recursive deconvolution for improved image quality. The system and reconstruction algorithm are applied to an experimental setting of detecting a concealed handgun in a package. Several practical considerations are discussed to ensure that the reconstruction and deconvolution can be applied successfully in retrieving good quality images. The experimental datasets and codes are available at https://adityamuppala.github.io/research/.

Index Terms—Circular synthetic aperture radars (CSARs), frequency-modulated continuous-wave (FMCW) radars, inverse synthetic aperture radars (ISARs), millimeter-wave imaging, 3-D imaging, wavefront reconstruction.

I. INTRODUCTION

IMAGING radars in the millimeter-wave and subterahertz band have become the technology of choice for concealed threat identification and standoff weapons detection in the past two decades [1], [2], [3], [4], [5]. Due to their nonionizing nature, they are much safer for repeated human exposure than X-rays. However, to this day, X-ray imaging remains the dominant technology for detection of weapons and contraband in packages and luggage at security checkpoints. X-ray systems offer high-resolution imaging capability with good penetration depth, but are limited by their large size and high cost ($50 000–$200 000). The high cost and size are due to the extensive shielding infrastructure needed to protect nearby humans from exposure to ionizing radiation. Therefore, for

applications where resolution requirements can be relaxed to ease the cost burden (< $1000), millimeter-wave imaging can offer a safe and viable alternative. Such a low-cost, moderate-resolution imaging system can be used for weapons detection in schools, office building, and public spaces, where the emphasis is on detecting large weapons, such as handguns and knives, rather than small blades or contraband. Furthermore, they can also be used in industrial settings for monitoring packing efficiency inside boxes, detecting damaged items, and identifying liquid leaks [6].

Driven by the growth in autonomous driving, millimeter-wave frequency-modulated continuous-wave (FMCW) radars, especially in the W-band (75–110 GHz), have become commercially successful and relatively cheap. Due to this, several moderate- to low-cost imaging systems have been proposed for concealed threat detection [7], [8]. All of them rely either on an array, increasing the system cost, or on mechanical raster scanning, increasing the imaging latency. This article proposes a system that breaks this tradeoff between system cost and imaging latency. The idea is to place the object under test on a precision high-speed turntable and illuminate it with a W-band FMCW radar system. Since the turntable is driven by a dc motor in closed loop feedback, the synthetic array can be formed in a fraction of a second. High-speed data acquisition can be achieved with a single transceiver, making the system both fast and low cost. The imaging latency is, therefore, limited by how fast the data can be processed into an image.

A circular synthetic aperture radar (CSAR) is known to capture sufficient information in the object's phase history to reconstruct an image [9]. The problem is akin to tomographic reconstruction, which has been widely studied in the SAR literature for linear and circular arrays [10], [11]. However, tomographic formulations of CSAR assume that the phase front at the target location is approximately planar, to admit reconstruction based on the inverse Radon transform. That assumption is valid for reconnaissance or topography mapping where the targets are far from the radar, but is invalid for near-zone imaging as in the case of millimeter-wave imaging.

Dropping the plane-wave phase front approximation and using a spherical phase front model, Soumekh developed a reconstruction algorithm for pulsed and stepped frequency CSAR that is fast [i.e., $\mathcal{O}(N^2(\log N)^2)$] [12]. However, pulsed and stepped frequency radars are not feasible for millimeter-wave imaging due to the bandwidth limitations of the analog-to-digital converters. In case of FMCW radars, since the target position shows up in both the frequency and phase of the downconverted IF signal, frequency-domain wavefront reconstruction cannot be directly applied [13]. The alternative is to use backprojection (or delay-and-sum)

reconstruction, which is very slow [14]. Here, we develop a time-domain wavefront reconstruction (TDWR) algorithm for FMCW inverse CSAR (ICSAR) that can be directly applied to the sampled time-domain intermediate frequency (IF) signals without the need for any preprocessing.

Furthermore, Soumekh's formulation is suitable for reconnaissance CSAR, where the array radius is much larger than the distance between the array plane and the target plane, and the beam area on the ground is very small compared with the array diameter. For near-zone millimeter-wave imaging, the radius is small, and the antenna beamwidth is large, causing the point spread function (PSF) to have undesirable sidelobes. This "dirty" PSF leads to several image artifacts that reduce image quality. We provide an extensive treatment of the deconvolution problem in sparse arrays and, in particular, circular arrays in [14]. To restore some of the image quality, we use a well-known recursive deconvolution algorithm called Coherent CLEAN [15]. Compared with our earlier work in [14], this article achieves faster deconvolution by deriving an analytical expression for the ICSAR PSF.

An additional motivation for developing a fast reconstruction algorithm for ICSAR is in the context of affine synthetic arrays using a dynamic dual reflector imaging system we developed in [16]. That system included a synthetic aperture of concentric circular arrays using a combination of an ellipsoidal subreflector and a conic main reflector. The synthetic array takes a CSAR geometry and our previous work relied on a backprojection algorithm for image reconstruction [3]. The FMCW-ICSAR reconstruction developed here would improve the computation speed and overall 3-D imaging time for such dual-reflector affine synthetic aperture radars.

The main contributions of this article are twofold: first, in evaluating millimeter-wave ICSAR as a viable solution for low-cost, high-speed concealed object detection, and second, in developing a fast ICSAR reconstruction algorithm for FMCW radars based on a TDWR with fast deconvolution. The FMCW radar architecture and phase calibration used in this article are presented in [13] and are not repeated here. The rest of this article is organized as follows. Section II introduces the FMCW-ICSAR signal model. Section III develops the TDWR algorithm. Section IV presents the PSF deconvolution. Section V concludes with the experimental results.

II. SIGNAL MODEL

Although CSAR and ICSAR have several differences in their practical implementations, as discussed in Section V, the resulting array geometries are identical, since they both form a circular synthetic aperture around the target. Therefore, the signal model developed here can also be applied to FMCW-CSAR. Fig. 1 shows a schematic of the ICSAR system. Consider a circular aperture of radius R_g centered at the origin and lying in the XY plane. Consider the $z = Z_c$ plane to be the 2-D imaging domain. Let $f(x, y)$ denote the target reflectivity of a point target located at $\vec{r} = (x, y, Z_c)$. Let the antenna location vector be $\vec{r}' = (x', y', 0)$, which is $(R_g, \phi', 0)$ in cylindrical polar coordinates. The FMCW transmitted pulse in terms of the fast time t is

$$s_t(t) = \exp\left(-j\left(\omega_c t + \frac{\gamma t^2}{2}\right)\right) \tag{1}$$

where $t \in [-T_p/2, T_p/2]$, ω_c is the center frequency in rad/s, and γ is the *chirp rate* [17]. Denoting the azimuthal position

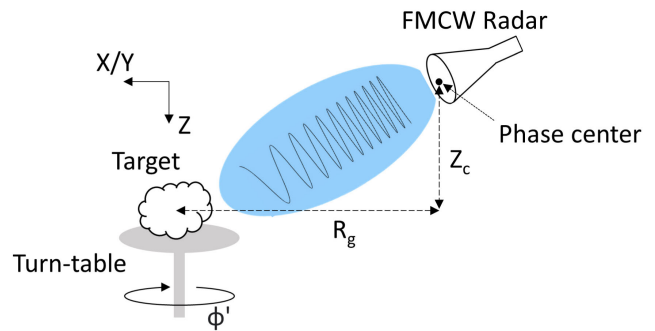Fig. 1.   Schematic of the proposed FMCW-ICSAR system.

of the transceiver (i.e., *slow time*) to be ϕ', the received signal after two-way propagation to a target point (x, y) at distance $r = ((x - R_g \cos\phi')^2 + (y - R_g \sin\phi')^2 + Z_c^2)^{1/2}$ is given by [17]

$$s_r(t, \phi') = \frac{1}{16\pi^2 r^2} \exp\left(-j\left(\omega_c\left(t - \frac{2r}{c}\right) + \frac{\gamma\left(t - \frac{2r}{c}\right)^2}{2}\right)\right). \tag{2}$$

After dechirping and low-pass filtering, the IF signal, also known as the beat signal, is an integral of signals reflected from the imaging domain [9]

$$s_b(t, \phi') = \int\int f(x, y) \frac{1}{16\pi^2 r^2}$$
$$\cdot \exp\left(-j\left(\frac{2\gamma r}{c}t + \frac{2\omega_c r}{c} - \frac{2\gamma r^2}{c^2}\right)\right) dx\, dy \tag{3}$$

where $(2\gamma r^2/c^2)$ is the *residual video phase* (RVP). For short-range FMCW-ICSAR imaging, as in the case of the system presented in this work, the RVP can be ignored, since $\gamma r^2 \ll c^2$. If the RVP cannot be ignored, it could be removed using a dispersive filtering step as described in [13] and [18]. Equation (3) takes the form

$$s_b(t, \phi') = \int\int f(x, y)\, g(x, y, \phi', t)\, dx\, dy \tag{4}$$

$$g(x, y, \phi', t) \triangleq \frac{1}{16\pi^2 r^2} \exp\left(-j\left(\frac{2\gamma r}{c}t + \frac{2\omega_c r}{c}\right)\right). \tag{5}$$

The Green's function can be simplified by using the following substitutions:

$$K_t \triangleq \frac{2\gamma}{c}t + \frac{2\omega_c}{c}, \quad x' = R_g \cos\phi', \quad y' = R_g \sin\phi' \tag{6}$$

$$g(x, y, \phi', t) = \frac{\exp\left(-j\left(K_t\sqrt{(x - x')^2 + (y - y')^2 + Z_c^2}\right)\right)}{16\pi^2\left((x - x')^2 + (y - y')^2 + Z_c^2\right)}$$
$$\triangleq \tilde{g}(x - x', y - y', t). \tag{7}$$

Substituting (7) in (4) formulates the ICSAR signal model as the following convolution-like integral:

$$s_b(t, \phi') = \int\int f(x, y)\, \tilde{g}(x - x', y - y', t)\, dx\, dy. \tag{8}$$

Image formation amounts to inverting the integral in (8) to obtain $f(x, y)$ from the measured $s_b(t, \phi')$.

III. ICSAR TDWR

The first step is to find the 2-D Fourier transform of the Green's function $g(x, y, \phi', t)$. One can approximate it using the method of stationary phase (MOSP) and space-shifting properties of the Fourier transform [19], [20]. Although MOSP is an approximation, the exact same result can also be obtained analytically [21, Eq.(8.2.25), Volume 2]. The result is given by

$$G(k_\rho, k_\phi, \phi', t) = \frac{j}{8\pi K_t Z_c} \exp\left(j\left(Z_c\sqrt{K_t^2 - k_\rho^2}\right)\right)$$
$$\cdot \exp\left(-jk_\rho R_g \cos(\phi' - k_\phi)\right) \qquad (9)$$

where k_ρ and k_ϕ denote polar spatial frequency coordinates.

Given the Fourier domain Green's function, we use the generalized Parseval's theorem to develop the image reconstruction method. This approach is based on Soumekh's CSAR reconstruction for stepped frequency and pulsed radars [12]. Applying Parseval's theorem, (4) takes the form

$$s_b(t, \phi') = \frac{1}{4\pi^2} \int \int F(-k_x, -k_y) G(k_x, k_y, \phi', t) \, dk_x \, dk_y \qquad (10)$$

where $F(k_x, k_y)$ denotes the spectrum of $f(x, y)$.

Since the constant terms do not matter in the reconstruction, we drop the $4\pi^2$ term for ease of notation. Converting from Cartesian to cylindrical coordinates in Fourier space (i.e., $(k_x, k_y) \rightarrow (k_\rho, k_\phi)$) takes $F(-k_x, -k_y)$ to $F(k_\rho, k_\phi \pm \pi)$. For simplicity, we drop $\pm\pi$. This rotates the final image by 180°, which can be compensated at the end

$$s_b(t, \phi') = \int \int F(k_\rho, k_\phi) G(k_\rho, k_\phi, \phi', t) k_\rho \, dk_\rho \, dk_\phi. \quad (11)$$

$$= \frac{j}{8\pi K_t Z_c} \int \int F(k_\rho, k_\phi) \exp\left(j\left(Z_c\sqrt{K_t^2 - k_\rho^2}\right)\right)$$
$$\cdot \exp\left(-jk_\rho R_g \cos(\phi' - k_\phi)\right) k_\rho \, dk_\rho \, dk_\phi. \qquad (12)$$

This equation can be reformulated as a linear *shift-varying* system as follows:

$$s_b(t, \phi') = \int G_0(t, k_\rho) \Gamma(k_\rho, \phi') dk_\rho \qquad (13)$$

where G_0 is the *unshifted* Green's function [i.e., setting $R_g = 0$ in (9)], which leaves $\Gamma(k_\rho, \phi')$ to be

$$\Gamma(k_\rho, \phi') = \int F(k_\rho, k_\phi) \exp\left(-jk_\rho R_g \cos(\phi' - k_\phi)\right) k_\rho \, dk_\phi. \qquad (14)$$

Equation (13) represents the forward model of wavefront reconstruction and can be inverted very efficiently by observing two facts. The first is that (13) is an expression for a linear shift-varying system with $G_0(t, k_\rho)$ as the impulse response or kernel. Therefore, its discrete version can simply be written as a product of two matrices[1]

$$S_b[t, \phi'] = G_0[t, k_\rho]\Gamma[k_\rho, \phi']. \qquad (15)$$

The second fact is that $G_0(t, k_\rho)$ is a highly oscillatory signal, from which it can be shown that the set of these signals is *nearly* orthogonal. Intuitively, the inner product integral of

---

[1]This article uses the notation $A[x, y]$ to represent the sampled 2-D matrix of a 2-D signal $A(x, y)$.

two highly oscillatory signals is nearly zero, because they do not share the same stationary phase point unless they are at the same frequency ([12], Appendix A). Since the amplitude factor in $G_0(t, k_\rho)$ can be made arbitrary by scaling $f(x, y)$, it can be chosen, such that each column of $G_0[t, k_\rho]$ has unit norm. Therefore, the matrix $G_0[t, k_\rho]$ is almost unitary, and its inverse can be approximated by its conjugate transpose $(G_0[t, k_\rho])'$. Equation (15) can, therefore, be (approximately) inverted as follows:

$$\Gamma[k_\rho, \phi'] = (G_0[t, k_\rho])' S_b[t, \phi']. \qquad (16)$$

An alternative approach is to use the truncated singular value decomposition (T-SVD) and the Moore–Penrose pseudoinverse to invert $G_0[t, k_\rho]$ [23]. The truncation tolerance for the singular values needs some trial and error and can be obtained by looking at the scree plot. Computationally, this is no different, since the inverse can be precomputed and stored. Now, $\Gamma[k_\rho, \phi']$ is known, and the next step is to invert (14) to obtain $F[k_\rho, k_\phi]$. Since (14) is a 1-D convolution over k_ϕ of $F(k_\rho, \phi')$ with $k_\rho \exp(-jk_\rho R_g \cos(\phi'))$, we deconvolve it using the following *matched filtering* approach:

$$F[k_\rho, \phi'] = \mathcal{F}_{\phi'}^{-1}\{\mathcal{F}_{\phi'}\{\Gamma[k_\rho, \phi']\}\mathcal{F}_{\phi'}\{\Gamma_0^*[k_\rho, \phi']\}\} \qquad (17)$$

where $\Gamma_0^*[k_\rho, \phi'] = k_\rho \exp[jk_\rho R_g \cos(\phi')]$ and $\mathcal{F}_{\phi'}$ denotes the 1-D fast Fourier transform (FFT) with respect to the ϕ' dimension. The last step is to reconstruct $f(x, y)$ from $F[k_\rho, \phi']$, which we accomplish very efficiently using an inverse nonuniform fast Fourier transform (NUFFT) [24], [25], [26]. Here, we use the Type-1 (nonuniform to uniform) NUFFT implemented by the accelerated Gaussian-gridding approach presented in [27].

We precompute $(G_0[t, k_\rho])'$ and $\mathcal{F}_{\phi'}\{\Gamma_0^*[k_\rho, \phi']\}$. Thus, the reconstruction algorithm simplifies to the matrix multiplication of (16), two 1-D FFTs, the matrix multiplication of (17), and a 2-D NUFFT. The overall computation complexity is $\mathcal{O}(N^2(\log N)^2)$, which is dominated by the final NUFFT step. This is much faster than backprojection or time-domain correlation, which have a computation complexity of $\mathcal{O}(N^4)$, demonstrating significant algorithmic gain in computation time. Later, in Section V, we show that the computational gain comes at no reduction in image quality compared with backprojection. One can reconstruct 3-D targets by treating each cross section (i.e., Z_c) separately. On a multicore system, this can easily be parallelized.

IV. PSF AND DECONVOLUTION

Although it looks like the ICSAR reconstruction reproduces $f(x, y)$ from $S_b[t, \phi']$, we are limited by the system's PSF. Unlike tomography, here, we are reconstructing $f(x, y)$ from spherical wave echoes that are sampled in a single plane that is offset from the plane of $f(x, y)$. For an exact reconstruction of $f(x, y)$, the sampled echoes would need to form a compact surface (such as a sphere or closed cylinder) that encloses $f(x, y)$ [28], [29]. A consequence of sampling only over a single ring is that the PSF is not a single point and instead has a main lobe and several side lobes. This nonideal or *dirty* PSF needs to be deconvolved from the final reconstructed image to obtain a clean image. An extensive treatment of the deconvolution problem for circular and sparse array synthetic aperture radars can be found in [14].

Recursive deconvolution algorithms, such as Coherent CLEAN and SATURN, have been shown to be successful in

deconvolving SAR data provided that the PSF is known [30]. The main drawback of these algorithms is that they are slow. For stepped frequency and pulsed radars, this is not a major concern, since imaging times are already severely limited by the slow data acquisition. However, FMCW ICSAR data can be acquired in under 1 s, and a fast deconvolution algorithm is necessary for high-speed system operation. In [14], we show that the recursive deconvolution algorithms rely on computing the localized PSF in different regions of the image at each step of the recursion. Originally, this was done by reconstruction algorithms, such as backprojection. Here, we derive an analytical form for the 2-D Fourier transform of the ICSAR PSF that we used to speed up the imaging time significantly.

A. ICSAR PSF

We start with a point target located at the origin, which will later be translated using the spatial translation properties of the Fourier transform. The measured signal from this target (see Section II) is given by

$$s_b(t, \phi') = \frac{\exp\left(-j\left(K_t\sqrt{R_g^2 + Z_c^2}\right)\right)}{16\pi^2\sqrt{R_g^2 + Z_c^2}}. \tag{18}$$

Using the backprojection (or delay-and-sum) reconstruction equation [14], the PSF for a target at origin is given by

$$h_0(x, y) = \int\int s_b(t, \phi') \exp(jK_t r)\, dt\, d\phi' \tag{19}$$

where $r = ((x - R_g\cos\phi')^2 + (y - R_g\sin\phi')^2 + Z_c^2)^{1/2}$. Next, we substitute (18) in (19) and evaluate the inner integral over time. Recalling that $K_t = (2\gamma/c)t + (2\omega_c/c)$ and the limits of the integral are $t \in [-T_p/2, T_p/2]$, we have

$$h_0(x, y) = \frac{jc}{2\gamma}\int\frac{e^{-jk_h(R_0-r)} - e^{-jk_l(R_0-r)}}{16\pi^2 R_0^2(R_0 - r)}\, d\phi' \tag{20}$$

where k_h and k_l are the upper and lower spatial frequency bounds of K_t and $R_0 \triangleq (R_g^2 + Z_c^2)^{1/2}$. To evaluate (20) analytically, we take the 2-D Fourier transform on both sides with respect to x and y. This pulls out the ϕ' dependence in r because of the spatial shifting property of the Fourier transform. The ϕ' integral then results in a Bessel function of the first kind $J_0(k_\rho R_g)$. The resulting expression is

$$H_0(k_x, k_y) = \frac{jc J_0(k_\rho R_g)}{16\pi\gamma R_0^2}$$
$$\cdot \mathcal{F}_{2D}\left\{\frac{e^{-jk_h(R_0-r_0)} - e^{-jk_l(R_0-r_0)}}{R_0 - r_0}\right\} \tag{21}$$

where $r_0 = (x^2 + y^2 + Z_c^2)^{1/2}$. The 2-D Fourier transform term is similar in form to the Green's function of (7). Therefore, it can be evaluated using MOSP [19]. The result is given by

$$H_0(k_x, k_y) = \frac{cZ_c J_0(k_\rho R_g)}{8\gamma R_0^2}$$
$$\cdot\left\{\frac{k_h e^{-j(Z_c k_h^z + k_h R_0)}}{k_h^z(k_h Z_c - R_0 k_h^z)} - \frac{k_l e^{-j(Z_c k_l^z + k_l R_0)}}{k_l^z(k_l Z_c - R_0 k_l^z)}\right\} \tag{22}$$

where $k_l^z = (4k_l^2 - k_x^2 - k_y^2)^{1/2}$ and $k_h^z = (4k_h^2 - k_x^2 - k_y^2)^{1/2}$. For the general PSF of a target located at (x', y'), we use the spatial shifting property of the Fourier transform, which gives

$$H(k_x, k_y, x', y') = \frac{cZ_c J_0(k_\rho R_g)}{8\gamma R_0^2}\exp(-jk_x x' - jk_y y')$$
$$\cdot\left\{\frac{k_h e^{-j(Z_c k_h^z + k_h R_0)}}{k_h^z(k_h Z_c - R_0 k_h^z)} - \frac{k_l e^{-j(Z_c k_l^z + k_l R_0)}}{k_l^z(k_l Z_c - R_0 k_l^z)}\right\}. \tag{23}$$

Although an approximation of the above result has been given in [31], it was developed in the context of determining the resolution of the main beam and not for deconvolution. Approximate results, that are only valid close to the main beam, are not sufficient for deconvolution, since they can lead to divergence or oscillations when used with iterative techniques [14]. Fig. 2 shows an image of the PSF magnitude in dB. In the discrete implementation, one can compute $H(k_x, k_y, x', y')$ over the grid points defined by (k_ρ, ϕ') over which $F[k_\rho, \phi']$ is defined in (17). This way, one could subtract the PSF before the last NUFFT step. Instead, we took the 2-D inverse FFT of (23) and performed the deconvolution on the reconstructed image. With this approach, care must be taken in handling the singularities that exist in (23). Alternatively, the singularities can be avoided by numerically computing the 2-D FFT in (21). Fig. 3 compares the analytical PSF and the numerical PSF obtained using TDWR. Despite the approximations made in the TDWR formulation, there is remarkable agreement between the two. The only deviation visible is below −60 dB. This level of accuracy in the PSF model is necessary for deconvolution.

The analytical form of the PSF provides a considerable speed benefit when implementing iterative (greedy) deconvolution algorithms, such as CLEAN or SATURN [14], [15], [30]. For example, in the case of CLEAN, using the analytical PSF makes the computation time of the deconvolution step almost as fast as the image reconstruction using TDWR.
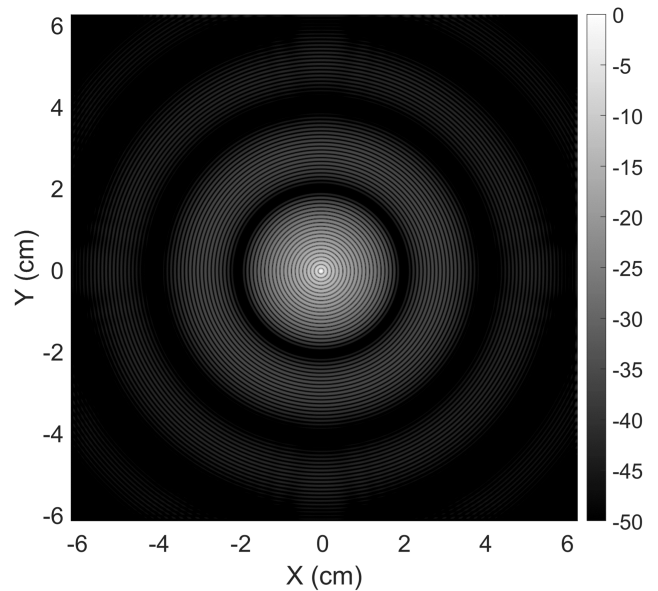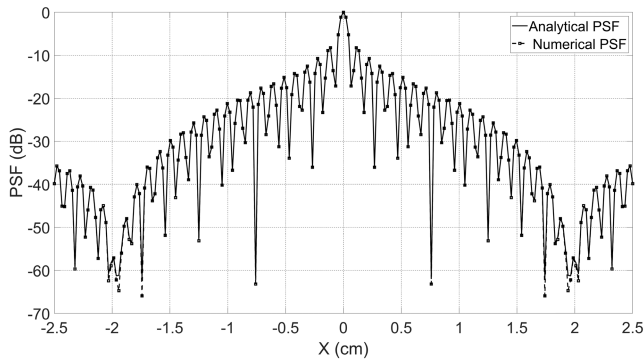

Fig. 2.   PSF from wavefront reconstruction. Target distance is 30 cm, and ICSAR radius is 100 cm with an operating bandwidth from 75.6 to 83.6 GHz. Intensity scale is in dB.

Fig. 3. PSF comparison between the numerical TDWR algorithm and the analytical expression.

Fig. 4. Constellation of 25 points using (a) TDWR and (b) TDWR + CLEAN.

A quantitative discussion on computation time is provided later in Section V. This provides an order of magnitude improvement in speed, since, otherwise, each iteration would take the same amount of time as a single image reconstruction. Since the basis of most deconvolution algorithms is knowing the PSF, the analytical form of the PSF developed here can be used to speed up many other deconvolution algorithms. In this article, we demonstrate its use with the CLEAN algorithm, because CLEAN has been shown to work well in the case of contiguous targets [30].

B. CLEAN Deconvolution

For the sake of completeness, we present the well-known CLEAN deconvolution algorithm using the wavefront reconstruction and the analytical PSF developed thus far. Full treatments of CLEAN can be found in [15], [30], and [14].

1) From the measured data $S_b[t, \phi']$, form an image using (16), (17), and the 2-D NUFFT.
2) Find the location (x', y') of the strongest peak from the absolute value of the complex image $|f(x, y)|$, and store the peak's complex magnitude.
3) Calculate the complex PSF due to this target using (23) and the 2-D IFFT. Scale it by the complex magnitude of the peak, and subtract it from the complex image.
4) Repeat steps 2) and 3), and save the location and complex magnitude of each peak until the residual image falls below a user defined threshold. Save the residual image.
5) Reconstruct the image by convolving the saved peaks with a Gaussian PSF that is devoid of sidelobes and add back the residual image.

Care must be taken in properly estimating the location of each peak. TDWR is limited in its final image resolution, which can miss the actual peak location. Therefore, the final TDWR image needs to be locally upsampled before performing peak search. Improperly estimating the peaks can cause CLEAN to oscillate or diverge with each iteration [14].

A simulation example of a standard 5×5 constellation of point targets is shown in Fig. 4. The deconvolution works very well, because the PSF of each target does not interact with the neighboring targets. In other words, the targets are sparsely populated, and the PSF is localized, making the deconvolution relatively easy. In cases where the PSF is much more spread out or if the targets are much closer, more sophisticated deconvolution algorithms, such as SATURN, are required. A full treatment of the phenomenology of deconvolution is
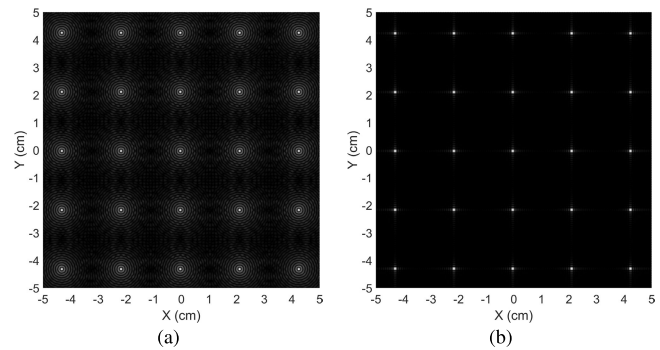
discussed in [14]. In short, the image quality from a dirty PSF is impacted in four ways as follows: 1) limited dynamic range; 2) image saturation; 3) target breakup; and 4) independent target correlation. Deconvolution can partially correct for some of these effects. However, the challenge with deconvolution is that, the choice of which algorithm to use and what values are to be chosen for the different hyperparameters depends strongly on not just the PSF but also the target being imaged. In this article, we use CLEAN, because, as we will show later in Section V, the image is dominated by a few scattering phase centers, and removing them is sufficient to produce a good quality image of the target.

V. EXPERIMENTAL RESULTS

A. System Considerations and Phenomenology

The signal model and reconstruction developed thus far have made several simplifying assumptions about the radiation and scattering characteristics of the system [32]. First, we have assumed omnidirectional radiation from the antennas. For broad-beam antennas, this approximation does not affect the reconstruction, since the amplitude variation with angle is small and does not impact the final image. However, when the beamwidth is small, it is important to account for windowing effects of the beam [12]. For our application of near-zone millimeter-wave imaging, it can be ignored, since the targets are close by, and the beamwidth is generally large ($\approx 60°$). We also ignored the RVP and phase nonlinearities generally associated with millimeter-wave FMCW radars. This is because phase nonlinearity effects are not significant for near-field imaging as long as the nonlinearity is not too unreasonable. If phase nonlinearity is significant, one can use the phase calibration procedure described in [13] to correct it before applying TDWR. Next, we have assumed the scattering characteristics of the target to be well approximated by a contiguous collection of point targets (i.e., omnidirectional scatterers), which do not vary over the entire band. Although this approximation is generally considered to be valid for real-world targets, it needs to be treated more carefully in the case of near-field ICSAR.

One main advantage of CSAR or ICSAR is that the target is illuminated from all azimuthal angles. This allows a reasonably accurate reconstruction under the assumption that all points on the target are "visible" from all directions, which is the case in most tomographic reconstruction problems. In ICSAR, however, if the slant height (Z_c) is close to zero, the radar can only see one side of the target. Therefore, features on the target that have a monostatic radar cross section (RCS)
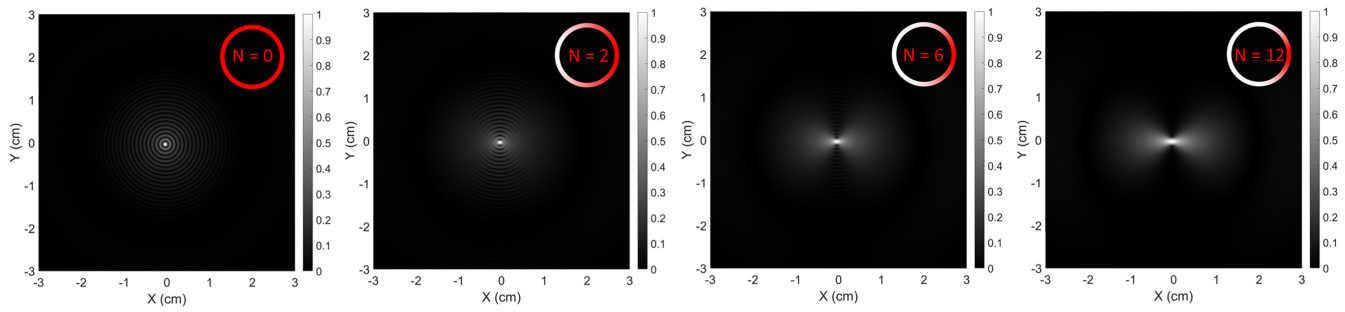
Fig. 5.   Point target images as a function of their monostatic RCS patterns. RCS is assumed to follow $\cos^N(\phi)$ pattern with $N = 0, 2, 6$, and 12.
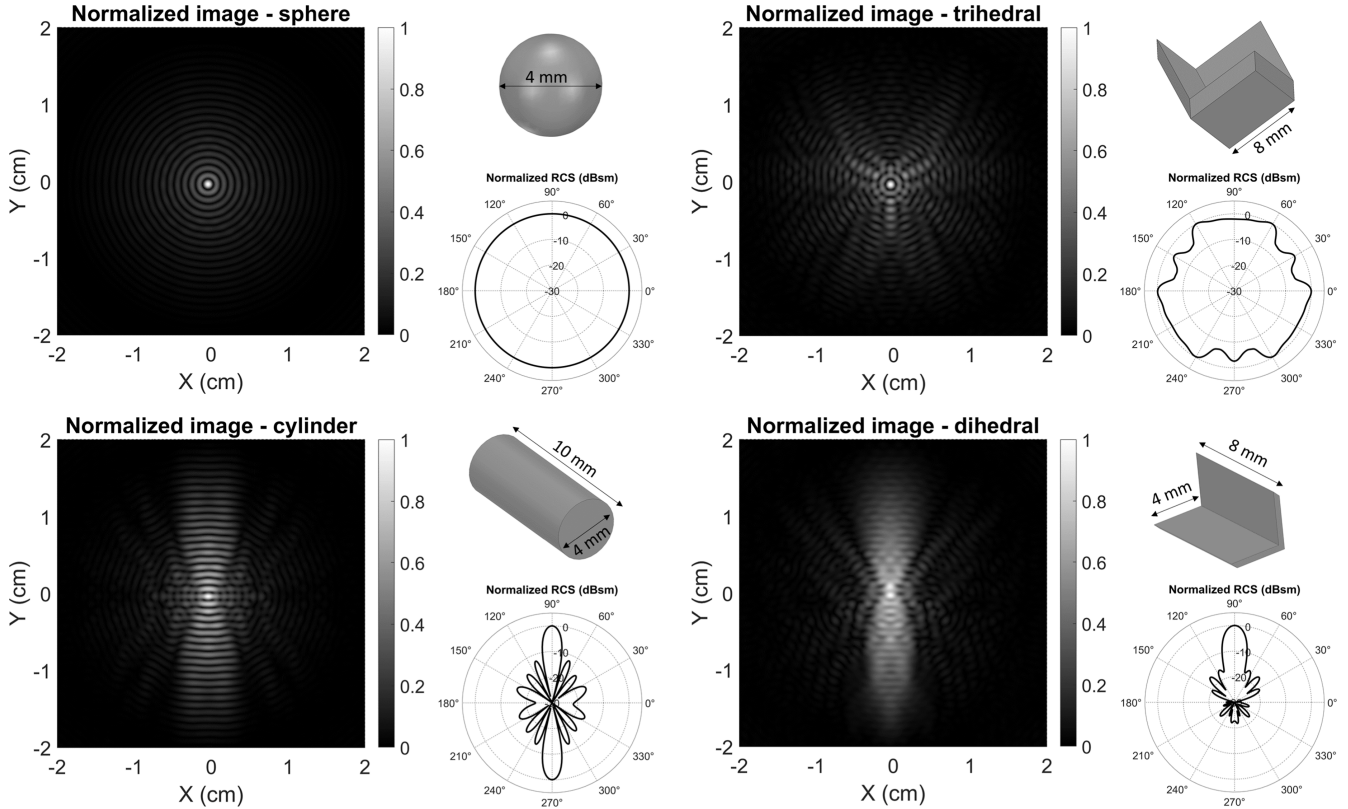

Fig. 6.   Radar cross section and corresponding images of different canonical targets. Elevation angle is 45°.

with a narrow azimuthal beamwidth will only be illuminated by a subset of the ICSAR measurements. Examples of such features include side walls and corners. The resulting response for these targets will deviate from the ideal azimuthally symmetric PSF derived earlier. This is demonstrated in Fig. 5, where the inset red/white circle represents the monostatic RCS of a point target. In these examples, the RCS is assumed to take the form $\cos^N(\phi)$ with $N = 0, 2, 6$, and 12. As the target response spreads in range, the monostatic RCSs of several canonical targets are simulated in a full-wave solver (ANSYS HFSS) and used to generate their corresponding images shown in Fig. 6. The main difference here is that these "extended" targets also have a phase associated with their RCS, which has a significant impact on the reconstructed images. The sphere has an image that resembles the system's ideal PSF, since its RCS is azimuthally symmetric. As this azimuthal symmetry is lost, the target images start to spread out in the directions of their RCS beams. As will be shown later, the smearing

out of the PSF, when an ideal point target is replaced with a real world target, leads to strong speckle artifacts in the reconstructed image.

Deconvolving such a "nonideal PSF" is much harder, since it depends on the target's scattering characteristics and location, which are not known a priori. Spatially varying blind deconvolution algorithms do exist, but they add significant computational burden due to their recursive nature [33]. A simpler solution is to compromise on the resolution and use a smaller R_g/Z_c ratio. If R_g/Z_c is made very small, the resolution of the system is reduced. Therefore, there is a tradeoff between reconstruction accuracy and resolution. As a general rule of thumb, we propose R_g/Z_c to be between 1 and 4.

Another consideration in ICSAR is the background clutter. This is one of the main differences between CSAR and ICSAR. In both cases, leakage between TX and RX will show up as a strong target at the origin, since it is constant over slow time. However, in ICSAR, all targets that are not
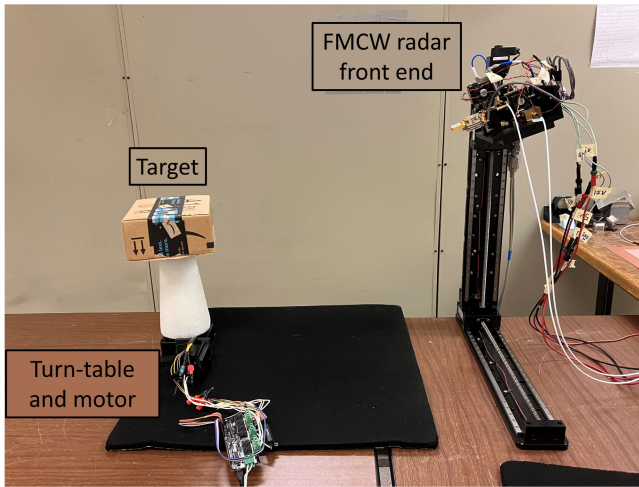
Fig. 7. Experimental setup of the ICSAR imaging system prototype.

rotating also have a constant response in slow time and, therefore, contribute to a strong target that appears at the origin in the final image. Fortunately, this strong false target has an ideal PSF, since its backscatter is constant in slow time. It should be removed using the deconvolution described earlier in Section IV. Vector background subtraction and time gating can also be used to reduce the impact of TX–RX leakage and background clutter.

B. Imaging Results

A custom W-band instrumentation radar is used for the ICSAR system setup. The bandwidth is 8 GHz from 75.6 to 83.6 GHz with an output power of 15 dBm. Full details of the system's architecture and calibration are available in [13] and are not repeated here in the interest of brevity. For accurate positioning of the target, a dc motor is connected to a rotation stage with a worm-gear coupling. The worm gear has a gear ratio of 180:1, and the dc motor is in closed loop feedback with an optical encoder. The angular accuracy and resolution of the positioning system are both less than 0.001°. The chirp duration is set to 48 μs with a pulse repetition interval of 50 μs. The rotation speed is set low at around 0.1 Hz due to the high worm gear ratio. Using a more accurate motor, the worm gear can be removed, in which case the rotation frequency can be increased up to 10 Hz. In practice, the rotation speed would have to be limited to around 1 Hz to avoid damage to the object being imaged. Data are collected at every 0.1° over 2400 time samples. The synchronization is done by the optical encoder, which sends a trigger pulse every 0.1° to both the chirp generator and the sampler. This makes the data acquisition independent from the instantaneous angular velocity of the motor. Fig. 7 shows the measurement setup.

To verify the performance of the system, we first reconstruct images of two canonical targets, a sphere and a dihedral corner reflector. Fig. 8 shows the reconstructed image of the sphere and its normalized RCS. There is some fluctuation in the RCS due to noise and weak reflections from the rotating pedestal. In this case, the ICSAR radius (R_g) and height (Z_c) are 20 and 20 cm, respectively, to keep the elevation angle consistent with the simulation results shown earlier in Fig. 6. This image also serves as the experimental PSF of the system, since a sphere

of any radius acts as a point target for a circular aperture due to the inherent azimuthal symmetry. From the PSF, the spatial resolution in both X and Y is found to be around 2 mm, which is commensurate with the spatial resolution of SAR in the near field (i.e., around $\lambda/2$). A derivation of this result is given in [13]. However, as mentioned earlier, the presence of the large sidelobes reduces the overall image quality compared with a system with the same resolution but without any sidelobes. The imaging dynamic range can also be obtained from the PSF [14]. It is the first sidelobe level and is equal to -10 dB, giving us an imaging dynamic range of 10 dB.

Fig. 8 shows the results of the dihedral corner. Note from the RCS plot that the backscatter has two peaks, one at 270° and another at 90°. This is different than the simulated RCS in Fig. 6 where only one peak is observed. In the experiment, the dihedral is sitting on a pedestal, which acts as a ground plane and creates the second weaker peak at 90°. The resulting image is similar to the simulated image of the dihedral with some differences introduced by the presence of the ground plane, noise, and background clutter.

Next, we conduct an imaging experiment of a concealed weapon inside a package. The target used is a 3-D printed GLOCK-19 replica that is coated with a copper spray and placed inside a cardboard box. The target is placed on a foam pedestal attached to the turntable, as shown in Fig. 7. The ICSAR radius (R_g) and height (Z_c) are 92 and 23 cm, respectively. Fig. 9 shows the reconstructed images using backprojection, TDWR, and TDWR + CLEAN. The image intensity is normalized to 1, and the scale is limited to values between 0.2 and 0.5 to improve the image quality. The total computed image size is 4096 × 4096 pixels, which covers a imaging domain of 50 × 50 cm. The images shown in Fig. 9 are cropped to 1000 × 1000 pixels for a closer view of the targets. The inset image shows a picture of the toy pistol used. The backprojection image and the TDWR image are remarkably identical. This is expected given that the PSF from these two methods is almost identical (refer to Fig. 3). The wavefront reconstructed image has several strong scattering points that dominate the image. The strongest scattering comes from the dihedral corner that forms between the trigger guard and the walls surrounding it. Locally, in this region, the image looks similar to the dihedral corner image of Fig. 8. There is also a strong scattering point at the origin, which corresponds to the background clutter and TX–RX leakage. Upon deconvolution, these scattering points are partially suppressed, and the entire extent of the target is more clearly visible, as shown in the TDWR + CLEAN image of Fig. 9. Another significant effect is the speckle that is caused by the sidelobes of the smeared out "nonideal PSF." From the final image, the shape of the pistol is easily identifiable with the naked eye. Finally, Fig. 10 shows the image of the target (reconstructed using TDWR) for different values of Z_c. When $Z_c = 23$ cm, the target comes into focus and is clear. For Z_c values greater than 23 cm, the target starts to spread out and goes out of focus. This phenomena arises due to the sparse nature of the CSAR geometry and is discussed in [9]. One approach to reducing this range spreading phenomena is to use multiple circular apertures of different radii as discussed in [3]. This comes at a higher system cost, but the same TDWR reconstruction can be used for faster processing.

TDWR and TDWR + CLEAN are implemented on a standard four-core 8-GHz desktop computer using MATLAB.
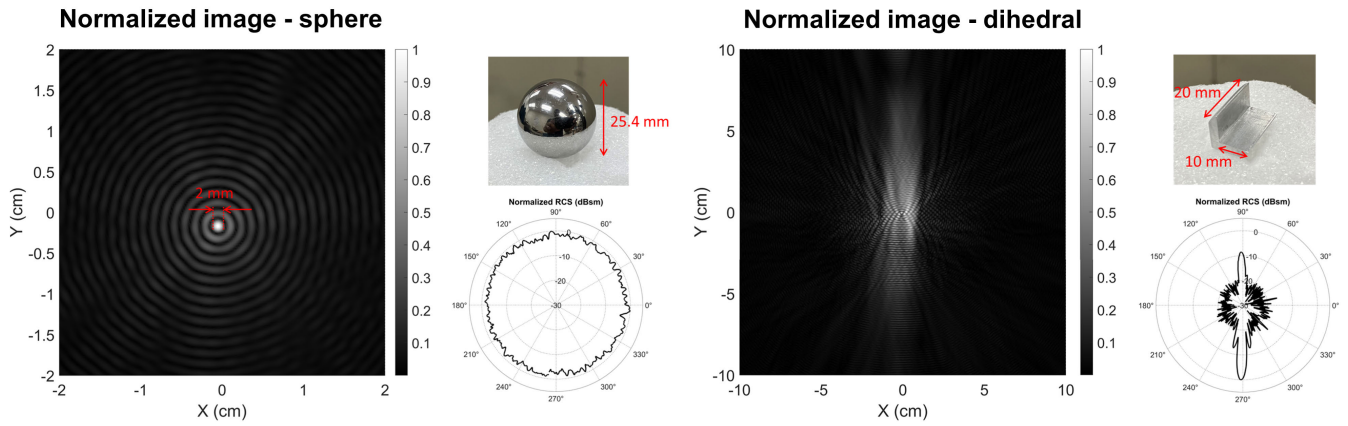
Fig. 8. Experimental imaging results of sphere (left) and dihedral (right) using TDWR.
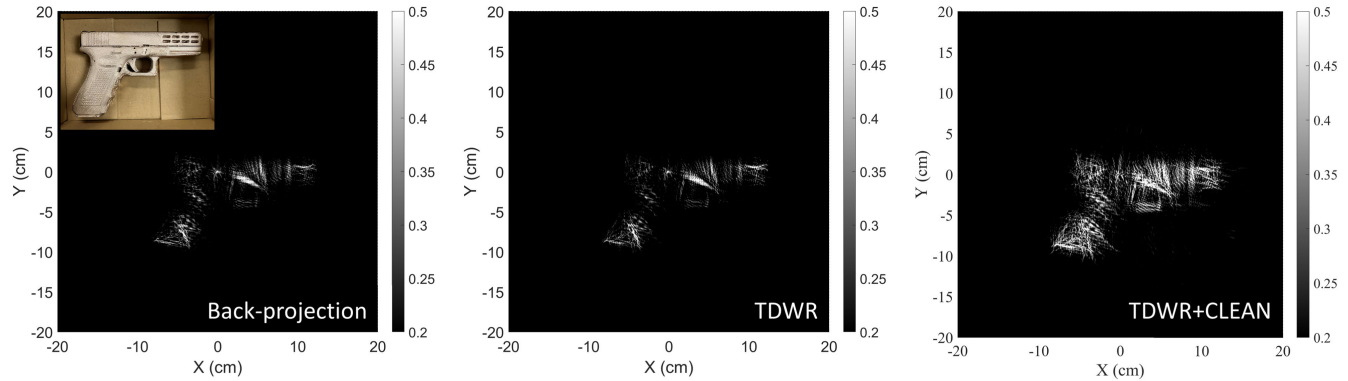

Fig. 9. Experimental imaging results from backprojection (left), TDWR (center), and TDWR + CLEAN (right). Computation time for TDWR is 8 s and for TDWR + CLEAN is 15 s.

TABLE I
COMPARISON OF MILLIMETER-WAVE RADAR IMAGING SYSTEMS

Journal and ref.	Architecture	Imaging time	Range resolution (cm)	Angular resolution	Frequency (GHz)	Size	Cost	Number of TX/RX
TMTT 2001 [2]	Linear array with SAR scan	Low (seconds)	2.5	0.8°×0.3°	27 - 33	Very large	High	64/64
TTST 2011 [34]	2-D mechanical scan	Low (seconds)	0.5	0.1°×0.1°	662 - 691	Large	Very high	1/1
TMTT 2011 [35]	MIMO array	Very low (< 1 second)	2	0.23°×0.23°	72 - 80	Medium	Very high	768/768
TGRS 2011 [5]	MIMO array with SAR scan	Moderate (minutes)	1	1.1°×1.1°	2.8 - 19.5	Large	Moderate	4/8
TMTT 2017 [36]	MIMO array	Very low (<1 second)	5	0.3°×0.3°	90 - 100	Small	High	22/22
TMTT 2022 [37]	Frequency steering with SAR scan	Low (seconds)	N/A	0.2°×0.2°	78 - 92	Large	Low	1/1
TMTT 2024 [13]	2-D SAR scan	High (hours)	2	0.2°×0.2°	76.5 - 84.5	Large	Very low	1/1
This Work	**Inverse Circular SAR**	**Low (seconds)**	**2**	**0.2°×0.2°**	**76.5 - 84.5**	**Medium**	**Very low**	**1/1**

The computation time for TDWR is 8 s, and that for TDWR + CLEAN is 15 s. The estimated imaging time using backprojection is around 225 h, which is five orders of magnitude slower than TDWR. This estimate is based on computing backprojection at a single point. In reality, backprojection can be limited to just the extent of the target,
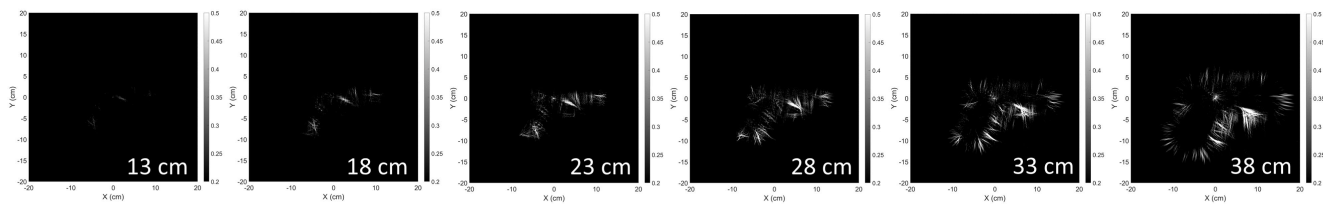
Fig. 10.   TDWR images of the pistol for different values of Z_c.

in which case the imaging time comes down to around 22 h, which is still four orders of magnitude slower than TDWR. The total data collection time and image processing time for the proposed prototype are around 25 s. With a faster motor and an FPGA, this total time can be brought down to under 1 s, which is comparable to current X-ray screening devices, thus making it a very fast and low-cost solution for package screening and concealed object imaging. Table I provides a comparison of different millimeter-wave imaging systems. The codes and associated datasets are available at https://adityamuppala.github.io/research/.

VI. CONCLUSION

This article presents millimeter-wave FMCW ICSAR as a practical and low-cost solution for high-speed imaging of concealed objects and packages. This is done by developing a fast time-domain imaging algorithm for FMCW-ICSAR based on wavefront reconstruction. Due to geometry constraints, the PSF is shown to have large sidelobes, which need to be removed. Deconvolution using recursive algorithms is proposed as a solution. To this effect, an analytical form for the PSF is derived and shown to have excellent agreement with the numerically computed PSF.

The imaging system is implemented using a W-band FMCW instrumentation radar with an operating bandwidth of 8 GHz. System-level considerations are discussed, and the implemented ICSAR prototype is used to image a concealed toy handgun inside a package at a standoff distance of around 1 m. A good quality image is obtained after wavefront reconstruction and deconvolution in which the gun is clearly identifiable. The total data acquisition time is around 10 s, and the reconstruction time on a standard desktop computer is around 15 s. The speed improvement compared with back-projection is around four orders of magnitude with almost no loss in image quality, which is verified by comparing the PSF from both these approaches.

REFERENCES

[1] R. Appleby and R. N. Anderton, "Millimeter-wave and submillimeter-wave imaging for security and surveillance," *Proc. IEEE*, vol. 95, no. 8, pp. 1683–1690, Aug. 2007.

[2] D. M. Sheen, D. L. Mcmakin, and T. E. Hall, "Three-dimensional millimeter-wave imaging for concealed weapon detection," *IEEE Trans. Microw. Theory Techn.*, vol. 49, no. 9, pp. 1581–1592, Sep. 2001.

[3] A. V. Muppala and K. Sarabandi, "Low-cost 3-D millimeter-wave concealed weapons detection using single transceiver affine synthetic arrays," *IEEE Trans. Microw. Theory Techn.*, vol. 71, no. 12, pp. 5445–5456, Dec. 2023.

[4] A. V. Muppala and K. Sarabandi, "A near-field 3-D imaging radar using a sparse spotlight MIMO array for weapons detection," in *Proc. IEEE Int. Symp. Antennas Propag. USNC-URSI Radio Sci. Meeting (USNC-URSI)*, Jul. 2023, pp. 739–740.

[5] X. Zhuge and A. G. Yarovoy, "A sparse aperture MIMO-SAR-based UWB imaging system for concealed weapon detection," *IEEE Trans. Geosci. Remote Sens.*, vol. 49, no. 1, pp. 509–518, Jan. 2011.

[6] A. Pedross-Engel, C. M. Watts, and M. S. Reynolds, "High-throughput 3-D millimeter-wave imaging of packaged goods: (Invited paper)," in *Proc. IEEE Radar Conf. (RadarConf)*, Sep. 2020, pp. 1–6.

[7] S. Devadithya, A. Pedross-Engel, C. M. Watts, N. I. Landy, T. Driscoll, and M. S. Reynolds, "GPU-accelerated enhanced resolution 3-D SAR imaging with dynamic metamaterial antennas," *IEEE Trans. Microw. Theory Techn.*, vol. 65, no. 12, pp. 5096–5103, Dec. 2017.

[8] D. R. Smith et al., "Security screening via computational imaging using frequency-diverse metasurface apertures," *Proc. SPIE*, vol. 10189, May 2017, Art. no. 101890B.

[9] M. Soumekh, *Synthetic Aperture Radar Signal Processing*, vol. 7. New York, NY, USA: Wiley, 1999.

[10] C. V. Jakowatz, D. E. Wahl, P. H. Eichel, D. C. Ghiglia, and P. A. Thompson, *Spotlight-Mode Synthetic Aperture Radar: A Signal Processing Approach: A Signal Processing Approach*. New York, NY, USA: Springer, 2012.

[11] D. C. Munson, J. D. O'Brien, and W. K. Jenkins, "A tomographic formulation of spotlight-mode synthetic aperture radar," *Proc. IEEE*, vol. 71, no. 8, pp. 917–925, Aug. 1983.

[12] M. Soumekh, "Reconnaissance with slant plane circular SAR imaging," *IEEE Trans. Image Process.*, vol. 5, no. 8, pp. 1252–1265, Aug. 1996.

[13] A. V. Muppala, A. Y. Nashashibi, E. Afshari, and K. Sarabandi, "Fast-Fourier time-domain SAR reconstruction for millimeter-wave FMCW 3-D imaging," *IEEE Trans. Microw. Theory Techn.*, early access, Jun. 5, 2024, doi: 10.1109/TMTT.2024.3406938.

[14] A. V. Muppala and K. Sarabandi, "SATURN: A double-recursive deconvolution algorithm for suppressing sidelobe effects in non-Nyquist SAR and MIMO imaging radars," *IEEE Trans. Geosci. Remote Sens.*, vol. 61, 2023, Art. no. 1001812.

[15] J. Tsao and B. D. Steinberg, "Reduction of sidelobe and speckle artifacts in microwave imaging: The CLEAN technique," *IEEE Trans. Antennas Propag.*, vol. AP-36, no. 4, pp. 543–556, Apr. 1988.

[16] A. V. Muppala and K. Sarabandi, "A dynamic dual reflector antenna for 4-D synthetic aperture radar imaging achieving a 0.4° pencil beam at 77 GHz," *IEEE Trans. Antennas Propag.*, vol. 70, no. 12, pp. 11301–11312, Dec. 2022.

[17] W. G. Carrara, R. S. Goodman, and R. M. Majewski, *Spotlight Synthetic Aperture Radar Signal Processing Algorithms*. Norwood, MA, USA: Artech House, 1995.

[18] A. Meta, P. Hoogeboom, and L. P. Ligthart, "Signal processing for FMCW SAR," *IEEE Trans. Geosci. Remote Sens.*, vol. 45, no. 11, pp. 3519–3532, Nov. 2007.

[19] A. Papoulis, *Systems and Transforms With Applications in Optics* (McGraw-Hill Series in System Science). New York, NY, USA: McGraw-Hill, 1968.

[20] J. M. Lopez-Sahcnez and J. Fortuny-Guasch, "3-D radar imaging using range migration techniques," *IEEE Trans. Antennas Propag.*, vol. 48, no. 5, pp. 728–737, May 2000.

[21] A. Erdélyi, W. Magnus, F. Oberhettinger, and F. G. Tricomi, *Tables of Integral Transforms*. New York, NY, USA: McGraw-Hill, 1954.

[22] User321120. *Hankel Transform of $exp(-a\sqrt{r^2+z^2}/\sqrt{r^2+z^2})$*. Math. Stack Exchange. Accessed: Mar. 20, 2024. [Online]. Available: https://math.stackexchange.com/q/4383994

[23] J. A. Fessler and R. R. Nadakuditi, *Linear Algebra for Data Science, Machine Learning, and Signal Processing*. Cambridge, U.K.: Cambridge Univ. Press, 2024.

[24] J. A. Fessler and B. P. Sutton, "Nonuniform fast Fourier transforms using min–max interpolation," *IEEE Trans. Signal Process.*, vol. 51, no. 2, pp. 560–574, Feb. 2003.

[25] A. H. Barnett, "Aliasing error of the $\exp(\beta\sqrt{1-z^2})$ kernel in the nonuniform fast Fourier transform," *Appl. Comput. Harmon. Anal.*, vol. 51, pp. 1–16, Mar. 2021. [Online]. Available: https://www.sciencedirect.com/science/article/pii/S1063520320300725

[26] A. H. Barnett, J. F. Magland, and L. af Klinteberg, "A parallel non-uniform fast Fourier transform library based on an 'exponential of semicircle' kernel," 2018, *arXiv:1808.06736*.

[27] L. Greengard and J.-Y. Lee, "Accelerating the nonuniform fast Fourier transform," *SIAM Rev.*, vol. 46, no. 3, pp. 443–454, Jan. 2004.

[28] L. A. Kunyansky, "Explicit inversion formulae for the spherical mean radon transform," *Inverse Problems*, vol. 23, no. 1, pp. 373–383, Jan. 2007, doi: 10.1088/0266-5611/23/1/021.

[29] D. Finch and S. K. Patch, "Determining a function from its mean values over a family of spheres," *SIAM J. Math. Anal.*, vol. 35, no. 5, pp. 1213–1240, Jan. 2004.

[30] R. Bose, A. Freedman, and B. D. Steinberg, "Sequence CLEAN: A modified deconvolution technique for microwave images of contiguous targets," *IEEE Trans. Aerosp. Electron. Syst.*, vol. 38, no. 1, pp. 89–97, Jan. 2002.

[31] A. Ishimaru, T.-K. Chan, and Y. Kuga, "An imaging technique using confocal circular synthetic aperture radar," *IEEE Trans. Geosci. Remote Sens.*, vol. 36, no. 5, pp. 1524–1530, Sep. 1998.

[32] K. Sarabandi, *Foundations of Applied Electromagnetics*. Ann Arbor, MI, USA: Michigan Publishing, 2022.

[33] S. Harmeling, H. Michael, and B. Schölkopf, "Space-variant single-image blind deconvolution for removing camera shake," in *Proc. Adv. Neural Inf. Process. Syst.*, vol. 23, J. Lafferty, C. Williams, J. Shawe-Taylor, R. Zemel, and A. Culotta, Eds., Red Hook, NY, USA: Curran Associates, 2010, pp. 1–9. [Online]. Available: https://proceedings.neurips.cc/paper_files/paper/2010/file/7f5d04d189dfb634e6a85bb9d9adf21e-Paper.pdf

[34] K. B. Cooper, R. J. Dengler, N. Llombart, B. Thomas, G. Chattopadhyay, and P. H. Siegel, "THz imaging radar for standoff personnel screening," *IEEE Trans. THz Sci. Technol.*, vol. 1, no. 1, pp. 169–182, Sep. 2011.

[35] S. S. Ahmed, A. Schiessl, and L.-P. Schmidt, "A novel fully electronic active real-time imager based on a planar multistatic sparse array," *IEEE Trans. Microw. Theory Techn.*, vol. 59, no. 12, pp. 3567–3576, Dec. 2011.

[36] D. Bleh et al., "*W*-band time-domain multiplexing FMCW MIMO radar for far-field 3-D imaging," *IEEE Trans. Microw. Theory Techn.*, vol. 65, no. 9, pp. 3474–3484, Sep. 2017.

[37] S. Li and S. Wu, "Low-cost millimeter wave frequency scanning based synthesis aperture imaging system for concealed weapon detection," *IEEE Trans. Microw. Theory Techn.*, vol. 70, no. 7, pp. 3688–3699, Jul. 2022.

Jeffrey A. Fessler (Fellow, IEEE) received the B.S.E.E. degree from Purdue University, West Lafayette, IN, USA, in 1985, and the M.S.E.E. and M.S. degrees in statistics, and the Ph.D. degree in electrical engineering from Stanford University, Stanford, CA, USA, in 1986, 1989, and 1990, respectively.

From 1985 to 1988, he was a National Science Foundation Graduate Fellow with Stanford University. From 1991 to 1992, he was a Department of Energy Alexander Hollaender Post-Doctoral Fellow with the Division of Nuclear Medicine. From 1993 to 1995, he was an Assistant Professor of nuclear medicine and the bioengineering program. He is a Professor with the Departments of Electrical Engineering and Computer Science, Radiology, and Biomedical Engineering. He is currently the William L. Root Professor of EECS with the University of Michigan, Ann Arbor, MI, USA. He has supervised doctoral research in PET, SPECT, X-ray CT, MRI, and optical imaging problems. His research interests include statistical aspects of imaging problems.

Dr. Fessler became a Fellow of the IEEE in 2006, for contributions to the theory and practice of image reconstruction. He was a recipient of the Francois Erbsmann Award for his IPMI93 presentation, Edward Hoffman Medical Imaging Scientist Award in 2013, and IEEE EMBS Technical Achievement Award in 2016. He was also a recipient of the 2023 Steven S. Attwood Award, highest honor awarded to a Faculty Member by the College of Engineering. He has Chaired the IEEE T-MI Steering Committee and the ISBI Steering Committee. He was the Co-Chair of 1997 SPIE Conference on Image Reconstruction and Restoration, a Technical Program Co-Chair of the 2002 IEEE International Symposium on Biomedical Imaging (ISBI), and the General Chair of ISBI 2007. He was an Associate Editor of IEEE TRANSACTIONS ON MEDICAL IMAGING, IEEE SIGNAL PROCESSING LETTERS, IEEE TRANSACTIONS ON IMAGE PROCESSING, and IEEE TRANSACTIONS ON COMPUTATIONAL IMAGING. He is an Associate Editor of *SIAM Journal on Imaging Sciences* and a Senior Associate Editor of T-CI.

Kamal Sarabandi (Life Fellow, IEEE) is the Fawwaz T. Ulaby Distinguished University Professor and the Rufus S. Teesdale Endowed Professor of Engineering at The University of Michigan, Ann Arbor, MI, USA. He has supervised 63 Ph.D. and numerous master's students and post-doctoral fellows. He led the Center for Microelectronics and Sensors funded by the Army Research Laboratory from 2008 to 2018 and is leading the Center of Excellence in Microwave Sensor Technology. He has published many book chapters, more than 325 papers in refereed journals, and more than 770 conference papers. He and his students are the recipients of 35 paper awards. His research areas of interest include microwave and millimeter-wave radar remote sensing, meta-materials, electromagnetic wave propagation, antenna miniaturization, and bioelectromagnetics.

Dr. Sarabandi served as a member for the NASA Advisory Council for two consecutive terms from 2006 to 2010 and the President for IEEE Geoscience and Remote Sensing Society from 2015 to 2016. He is a Fellow of American Association for the Advancement of Science (AAAS) and the National Academy of Inventors. He is also a member of the National Academy of Engineering. He is the past Chair of Commission F of USNC/URSI and serves as a member of the AdCom for the IEEE Antennas and Propagation Society. His contributions to the field of electromagnetics have been recognized by many awards, including the Humboldt Research Award, the IEEE GRSS Distinguished Achievement Award, the IEEE Judith A. Resnik Medal, the IEEE GRSS Education Award, the NASA Group Achievement Award, and many other awards from the University of Michigan. He received the esteemed recognition of being chosen as one of the Inaugural Members of the "Legends of Electromagnetics" by the IEEE Antennas and Propagation Society. He was a recipient of the prestigious Ellis Island Medal of Honor.

Aditya Varma Muppala (Graduate Student Member, IEEE) received the B.Tech. degree in electronics and communication engineering from Vellore Institute of Technology, Vellore, India, in 2018, and the dual M.S. degree in electrical engineering and mathematics from the University of Michigan, Ann Arbor, MI, USA, in 2020 and 2023, respectively, where he is currently pursuing the Ph.D. degree in electrical engineering.

His research interests include millimeter-wave imaging radars and antennas, subterahertz integrated circuits, array processing algorithms, and microwave measurement techniques.

Mr. Muppala received the 2023–2024 Rackham Predoctoral Fellowship, the 2024 College of Engineering's Towner Prize for Outstanding Graduate Student Instructor, and the 2024 College of Engineering's Towner Prize for Outstanding Ph.D. Research.